ACS APPLIED MATERIALS & INTERFACES

Research Article

Cite This: ACS Appl. Mater. Interfaces 2019, 11, 18233−18241

www.acsami.org

Reference-Free Traction Force Microscopy Platform Fabricated via Two-Photon Laser Scanning Lithography Enables Facile Measurement of Cell-Generated Forces

Omar A. Banda,[†] Chandran R. Sabanayagam,[‡] and John H. Slater*[,†]

[†]Department of Biomedical Engineering, University of Delaware, 5 Innovation Way, Newark, Delaware 19711, United States

[‡]Delaware Biotechnology Institute, University of Delaware, 15 Innovation Way, Newark, Delaware 19711, United States

Supporting Information

ABSTRACT: Cells sense and respond to the physical nature of their microenvironment by mechanically probing their surroundings via cytoskeletal contractions. The material response to these stresses can be measured via traction force microscopy (TFM). Traditional TFM platforms present several limitations including variable spatial resolution, difficulty in attaining the full three-dimensional (3D) deformation/stress profile, and the requirement to remove or relax the cells being measured to determine the zero-stress state. To overcome these limitations, we developed a two-photon, photochemical coupling approach to fabricate a new TFM platform that provides high-resolution control over the 3D placement of fluorescent fiducial markers for facile measurement of cell-generated shear and normal components of traction forces. The highly controlled placement of the 3D marker array provides a built-in, zero stress state eliminating the need to perturb the cells being measured while also providing increased throughput. Using this platform, we discovered that the magnitude of cell-generated shear and normal force components are linked both spatially and temporally. The facile nature and increased throughput of measuring cell-generated forces afforded by this new platform will be useful to the mechanotransduction community and others.

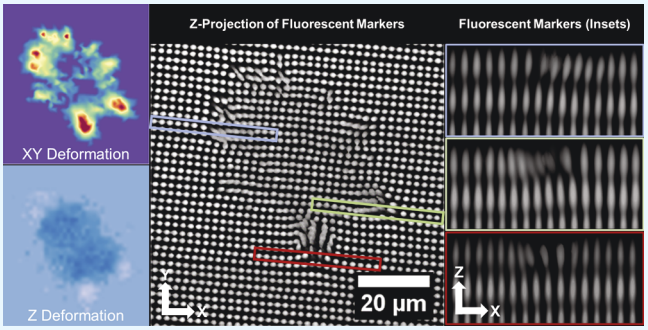

KEYWORDS: *hydrogel, cytoskeletal tension, multiphoton lithography, mechanotransduction, cell patterning*

INTRODUCTION

Traction force microscopy (TFM) has become the standard method to measure cell-generated forces and investigate the role these forces play in mediating cell behavior. TFM has been implemented to investigate the influences of cytoskeletal tension and/or traction forces in regulating cell proliferation,[1−3] differentiation,[4−9] migration,[10−12] nuclear polarization,[13] nuclear deformation,[14−16] and reaction to drugs.[17] Although cell-generated shear components of traction are usually measured, the magnitude of the out-of-plane, normal components can reach 50% of in-plane, shear components.[12,18] Normal components of traction play an important role in cellular processes including leukocyte extravasation[19] and may also influence cell fate via nuclear deformation and chromatin remodeling.[14,15,20,21] Accordingly, the ability to accurately and easily measure out-of-plane, normal components, along with shear components, is of great interest to many areas of research.

The most common platform capable of measuring out-of-plane, normal tractions utilizes protein- or peptide-functionalized elastomeric materials, usually polyacrylamide, containing embedded micro- or nanometer-sized fluorescent spheres that act as fiducial markers to measure material deformation.[18,22,23] These platforms are straightforward to fabricate and characterize and provide high-resolution traction measurements through the use of densely packed fluorescent spheres.[24] A limitation of this approach is the lack of control over fiducial marker placement and spacing. This lack of control can induce a number of spacing-related issues.[25] For example, markers may be too close together to be accurately resolved or too far apart as to create unusable regions, together inducing regionally biased resolution in material deformation measurements and subsequent force/stress calculations. Random marker placement also necessitates acquisition of a zero-stress state reference image to be registered with the deformation images for displacement measurements, requiring physical removal of the cells being examined or chemical perturbation to relax their cytoskeletal tension. This necessity hinders long-term cell studies and prevents subsequent cellular analyses.

To overcome some of these limitations, several reference-free platforms have been generated using micromolding and other high-resolution fabrication techniques.[17,26−29] The most

Received: March 11, 2019
Accepted: May 2, 2019
Published: May 2, 2019

DOI: 10.1021/acsami.9b04362
ACS Appl. Mater. Interfaces 2019, 11, 18233−18241

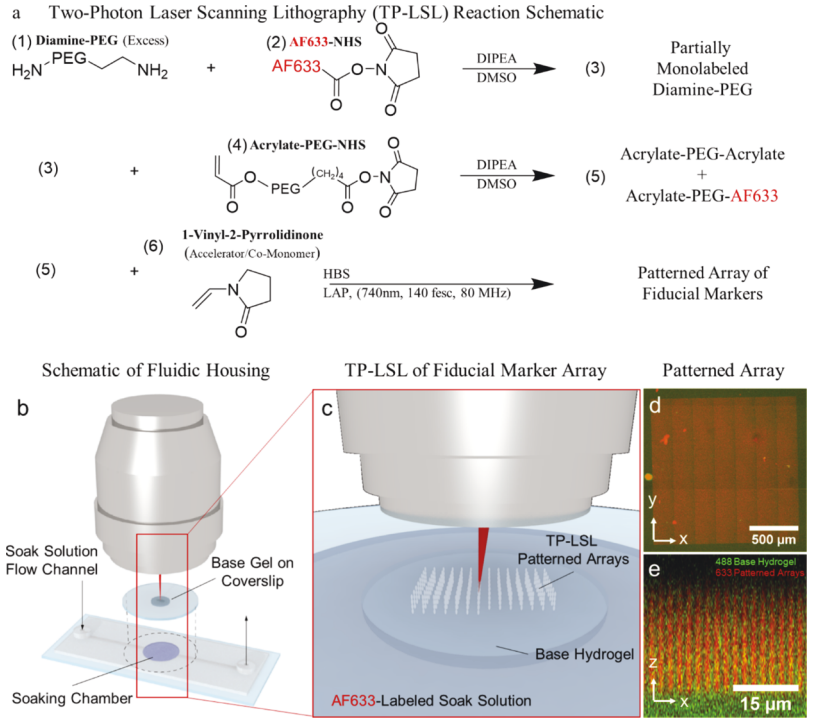

Figure 1. Fabrication of the reference-free TFM platform. (a) Fluorophore-labeled PEG used to fabricate fiducial markers is synthesized by coupling a diamine-PEG to either an acrylate and a fluorophore or two acrylates using NHS esters. (b,c) Resulting acrylated-PEG species are photocoupled into a preformed hydrogel by soaking the hydrogel in a solution containing the PEG species, a radical generating photoinitiator (LAP), and a comonomer (NVP). (d,e) Resulting fiducial markers are patterned in large arrays within the upper ~20 μm of the base hydrogel.

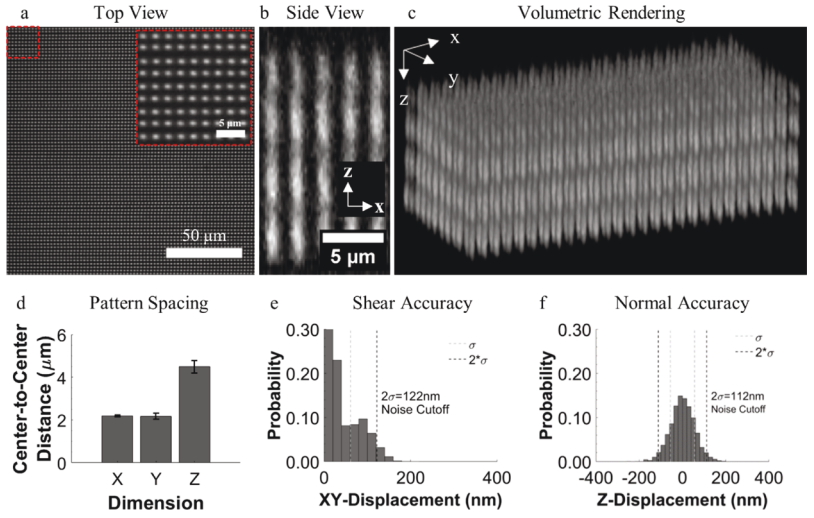

Figure 2. Characteristics of the fiducial marker array. (a) Single view field of a patterned region with an inset demonstrating the consistency of the patterns. (b) Profile view and (c) volumetric rendering of a patterned region demonstrating the intensity profile of fiducial markers through the *Z*-direction that allows for centroid localization based on intensity fluctuations. (d) Mean spacing between fiducial markers in the patterned array. (e,f) Histograms demonstrating the accuracy of reference lines as a true reference, displayed as the probability of measuring fiducial marker displacement in a nondeformed marker array.

commonly implemented method in this category utilizes micromolded pillar arrays to approximate cellular tractions based on the deflection of pillars in response to cell-generated tension. The reference position of the surface of the pillars is approximated based on the location of the pillar base. Pillar-based methods greatly facilitate measures of cell-induced shear components but are limited to two-dimensional (2D) measures. Reference-free platforms capable of measuring out-of-plane deformations implement patterned arrays of fluorescent fiducial markers on the surface of an elastomeric substrate with high spatial resolution and fidelity. The patterned marker surface array can serve as a built-in, implied, zero-stress reference state. The implied reference provides the ability to measure cell-induced material deformation using a single three-dimensional (3D) image acquisition, without physically removing or chemically perturbing the cells, thereby enabling facile use of standard cell analysis techniques,

DOI: 10.1021/acsami.9b04362
ACS Appl. Mater. Interfaces 2019, 11, 18233−18241

including immunofluorescence labeling, in combination with TFM.[26,30]

We developed an alternative reference-free platform using a photolithographically patterned hydrogel containing a built-in, implied reference state to measure the complete 3D material deformation profile induced by cells. The platform allows for continuous capture of material deformation without chemically relaxing or physically removing the cells. This facilitates temporal measurements of the same cell population over extended time as well as the ability to analyze a relatively large cell population providing higher throughput. The platform utilizes a 3D array of fluorescent fiducial markers embedded in a base hydrogel. Two-photon laser scanning lithography (TP-LSL)[31−36] is implemented to photocouple fluorescently labeled, poly(ethylene glycol) monoacrylate macromers into a base hydrogel composed of poly(ethylene glycol) diacrylate (PEGDA) (Figure 1). The resulting markers are ellipsoidal in shape with a 3D profile dictated by the point spread function of the pulsed laser. Reference positions for displaced markers are approximated using linear fits of surrounding nondisplaced markers resulting in a digital reconstruction of the zero-stress state. We demonstrate that using this implied reference state allows facile measurement of shear and normal components of cell-generated tractions using a single volumetric image stack. Using this platform, we quantified material deformation profiles and forces induced by individual human umbilical vein endothelial cells (HUVECs) as well as small HUVEC clusters. Consistent with a previous study, we observe that the extent of the shear component of traction generated by individual cells is positively correlated with increased spreading.[37] We further demonstrate that the normal component induced by individual cells follows a similar trend and that shear and normal components are tightly linked both in magnitude and temporally. Cell clusters display weaker correlations of shear and normal components of tractions with increased area, but the magnitude of shear and normal components are still tightly linked. We also demonstrate the ability to generate single-cell patterns via a second round of TP-LSL to photocouple PEG monoacrylates functionalized with integrin-binding peptide, arginine-glycine-aspartic acid-serine (RGDS), to the hydrogel surface to control cell shape and spreading.

RESULTS

The platform consists of a base PEGDA hydrogel containing an embedded array of ellipsoidal fluorescent fiducial markers with Gaussian-like intensity profiles (Figure 2a−c). We chose PEGDA because of its protein-repulsive properties, biological inertness, and ease of chemical and mechanical manipulation. The size, shape, and intensity profile of the patterned fiducial markers are dictated by the numerical aperture of the objective as well as the intensity of the focused laser beam. Using a 740 nm, 140 fs pulse width, Ti:S laser operating at 80 MHz with a fluence of 3.7 nJ μm^{-2} focused through a 1.2 numerical aperture water immersion objective resulted in ellipsoidal features with full-width, half maximum dimensions of 0.84 ± 0.11 μm in XY and 3.73 ± 0.30 μm in Z. Marker spacing was prescribed in the X-direction by a digital mask (2.12 μm), in Y by an automated image tiling step size (2.12 μm), and in Z by an automated Z-stepping size for the objective turret motor (3.5 μm). The center-to-center marker spacing varied slightly from the dictated values as the spacing precision was dependent on the mode of stepping (image-guided galvometers vs stage motor vs objective turret motor). A spacing in X of 2.19 ± 0.04 μm, Y of 2.17 ± 0.14 μm, and Z of 4.50 ± 0.30 μm was typically achieved (Figure 2d), with a corresponding 2D fiducial marker density of 0.21 markers μm^{-2} in XY and 3D density of 0.05 markers μm^{-3}.

To determine the accuracy of using reference line fitting to establish marker centroid positions, the deviation of fiducial marker centroids in nonstressed hydrogels, without cells, was measured (Figure 2e,f; Figure S1), as well as in nondeformed regions sufficiently far enough away from cells as to not be displaced. The value representing two standard deviations from the mean displacement magnitude in each patterned region was used to characterize the accuracy and to set a lower limit threshold of displacement magnitude, which would reliably yield displacements of the correct orientation. Displacements falling below the threshold were treated as noise and suppressed. The threshold value was updated for each patterned region to account for possible variability. Typical accuracies were 127 ± 17 nm in the XY plane and 140 ± 22 nm in Z.

To quantify stiffness of the hydrogels for traction force calculations, nanoindentation experiments were performed using a Bruker Bioscope Catalyst BioAFM (Figure 3). All

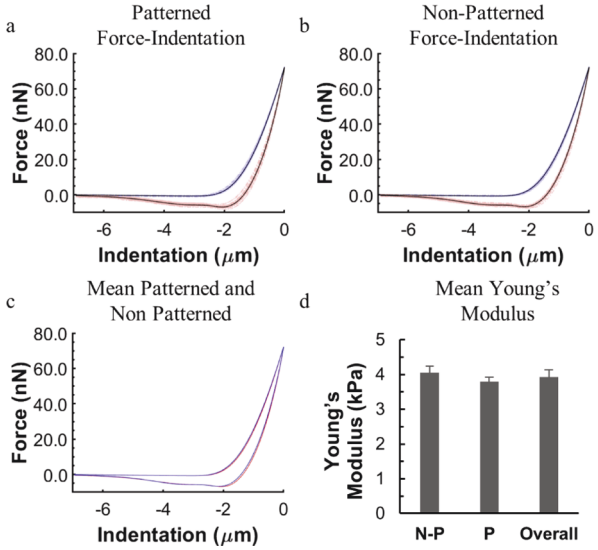

Figure 3. Nanoindentation of PEGDA hydrogels to measure surface elasticity. Force indentation curves of (a) patterned and (b) nonpatterned hydrogels. Blue lines indicate approach, red lines indicate retraction, and black lines represent the average profile. (c) Overlay of the average indentation curves shows minimal difference between patterned and nonpatterned hydrogels. (d) Average Young's modulus determined from a Hertzian contact model for nonpatterned (N-P), patterned (P), and all regions (overall). n = 129 (66 patterned, and 63 nonpatterned).

curve fitting was performed using the Bruker NanoScope Analysis (see the Supporting Information). Of particular interest was whether addition of fluorescent fiducial markers had a measurable impact on hydrogel elasticity. The surface moduli for the patterned and nonpatterned hydrogels were 3.79 ± 0.12 and 4.05 ± 0.18 kPa, respectively. Although this difference was statistically significant, the functional impact of the difference was ignored because of its low magnitude. To account for the possibility that the observed differences were simply due to local variations in surface elasticity of the base

DOI: 10.1021/acsami.9b04362
ACS Appl. Mater. Interfaces 2019, 11, 18233−18241

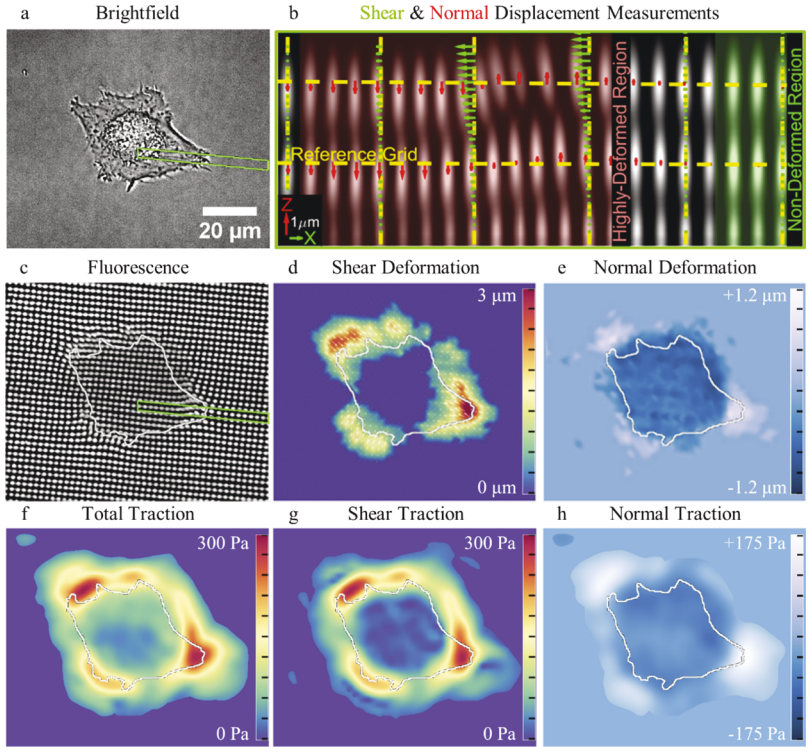

Figure 4. Measuring 3D cell-induced hydrogel deformation and tractions. (a) Brightfield image of a HUVEC seeded on the surface of a patterned gel. (b) *XZ* profile view of the inset [green box in (a)] demonstrates how reference lines are used to measure shear and normal fiducial marker displacement. (c) *Z*-projection of the fluorescent markers below the adherent HUVEC demonstrates a clear representation of the measured displacements. Heatmaps of (d) shear and (e) normal deformation. Surface tractions are displayed as (f) total magnitude, (g) magnitude of shear component of tractions, and (h) normal component of tractions.

hydrogel, a Young's modulus of 3.9 kPa representing an average of all measures and which is within 5% of all measured means was used for traction calculations.

To approximate the zero-stress state marker positions for a displacement data set, we interpolated reference positions for displaced markers from linear fits of nondisplaced markers within the same row or column (Figure 4b; see the Supporting Information). For any given marker, the intersection of linear fits of nondisplaced markers in the *X*-direction (rows) and in the *Z*-direction (columns) provided the 3D, nonstressed, reference coordinates needed to measure marker displacement. The reference lines running axially (*Z*-direction) through the hydrogel were used to measure the shear displacement in the *XY* plane. A depth of 12 μm into the hydrogel, from the surface, was sufficient to reach nondisplaced markers with *XY* coordinates that represented the zero-stress state location of displaced markers. To measure normal marker displacement, linear reference fits parallel to the hydrogel surface (*X*-direction) were used. A dilation of the cell boundary in *XY* of 8.13 μm was sufficient to encompass, on average, >90% of all hydrogel deformation, so all markers beyond the boundary were designated nondisplaced for fitting reference lines. To convert marker displacements to surface tractions, we implemented a 3D TFM algorithm which utilizes a linear elastic material model with Young's modulus of 3.9 kPa and ν = 0.2 (Figure 4f–h).[38] A Poisson's ratio of 0.2 was chosen as it accurately describes small hydrogel surface deformations.[39−41] Prior to conversion, unfiltered deformation data were interpolated to a grid spacing equal to the sampling density of the fiducial marker arrays, which served as the input to the TFM code.

Using this new platform, many cells can be measured without concern for maintaining positional accuracy to collect a nonstressed, reference state image, thereby allowing for higher throughput. To demonstrate this, data were collected from more than 50 individual cells and 9 cell clusters over a 24 h period, including several time-lapse studies. As metrics to describe the total material deformation induced by a cell, surface displacements were interpolated to a grid spacing matching the sampling density of the original marker arrays. The sum of the displacement magnitudes in the *XY* plane and in *Z* are referred to as the sum of shear displacement and sum of normal displacement, respectively. To validate the platform, we reproduced a previously reported trend of linearly increased shear with increased cell spreading (Figure 5a).[37] As the platform allows facile measurement of normal components, we also examined this relationship and demonstrated that normal deformation and force follow similar linear trends with increased cell spreading (Figure 5b,h). To further investigate the relationship between shear and normal traction components, we examined their relative magnitude, spatial distribution, and temporal behavior. We found a positive correlation between shear and normal deformation and traction components for all cells measured, where the slope of a linear regression was 1.39 and 1.13 for the deformation and forces, respectively (Figure 5c). This prompted us to investigate how the normal and shear components were related spatially. The largest material deformation occurs at the cell periphery with shear components oriented toward the cell interior, upward normal components occurring distally, and downward normal components proximally (Figure 5d–f). The relative spatial organization of shear and normal components suggests a

DOI: 10.1021/acsami.9b04362
ACS Appl. Mater. Interfaces 2019, 11, 18233−18241

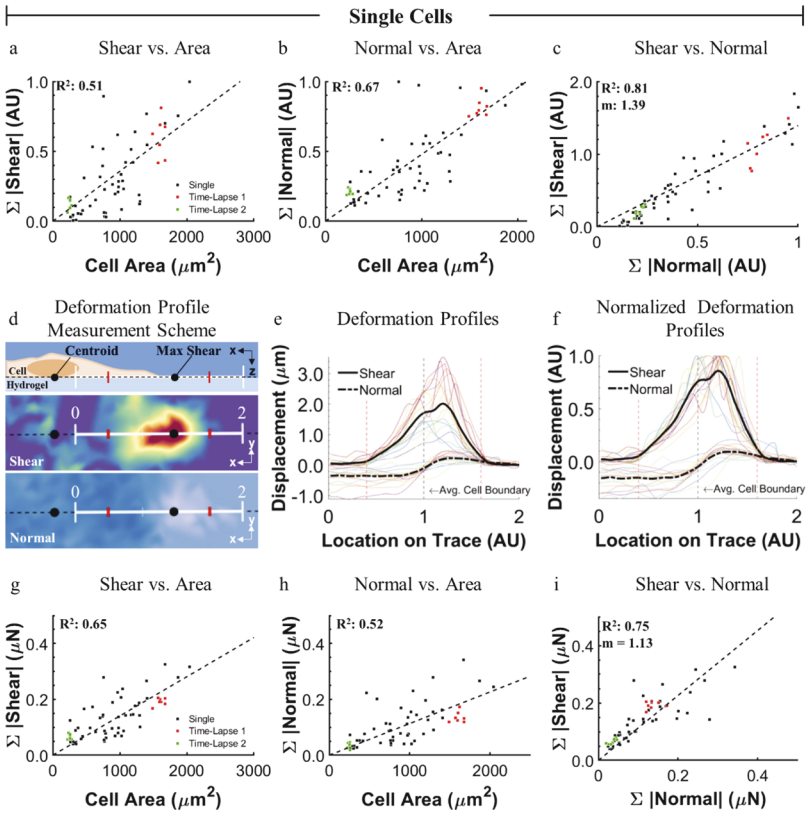

Figure 5. Magnitudes and distributions of cell-induced hydrogel deformations and forces. Positive linear correlations exist between both (a) shear and (b) normal deformation with increased cell spreading for individual single cells. Black markers represent different individual cells and red and green markers are time-lapse measures of specific cells. (c) Strong linear correlation was observed between the sum of shear and normal deformation magnitudes (normalized to highest normal magnitude). n = 60 data points for (a–c). The distribution of shear and normal deformation was measured along a trace from the cell center through the maximum shear. (d) Lengths of the profiles were normalized so that the proximal and distal locations where the magnitude of shear was 20% of the maximum occurred at 0.4 and 1.6 (red ticks). (e,f) 22 profiles of shear and normal deformation, with the average plotted in black. The transition from negative to positive normal deformation occurs at the cell boundary, with maximum shear coinciding with maximum positive normal deformation. (g–i) Calculated shear and normal traction components corresponding to (a–c), respectively.

rotational moment occurring about the location of maximum shear, likely at focal adhesions, as has been previously reported.[12,18,42] The observed trends in displacement data held true for the converted traction data (Figure 5g–i). Time-lapse studies (Figure 6, Movies S1 and S2) demonstrate that the shear and normal traction components vary with time (Figure 6a,b) but that the relative ratio of shear to normal components stays nearly constant (Figure 6c), indicating that normal and shear components are linked in magnitude even temporally. We applied the same analysis to cell clusters (Figure 7). Interestingly, although small clusters did not always exhibit the same spatial distribution of shear and normal components as observed in individual cells (Figure S2), the overall ratio of shear to normal was consistent with that of individual cells with a linear regression slope of 1.39 and 1.08 for deformation and forces, respectively (Figure 7c). In addition, we observed the highest magnitude of the in-plane component of cellular tractions at the periphery of cell clusters, suggesting that cell–cell junctions propagate cell–matrix loads between cells in a cluster, consistent with previous studies.[43–45]

A common technique often coupled with TFM is micro-contact printing,[6,9,46,47] which provides control over adhesion ligand availability and subsequently cell spreading and shape. Using TP-LSL, the same control can be achieved at the hydrogel surface. The protein-repulsive nature of PEG provides a nonadhesive background for patterning cells. We implemented a second round of TP-LSL to photocouple an RGDS-functionalized PEG monoacrylate macromer to the surface of the TFM platform to generate arrays of single-cell patterns (Figure 8). We demonstrate the ability to culture adipose-derived stem cells on 50 μm diameter circular patterns and elongated, obround patterns which induced a high-tension state with strain concentrated at the rounded narrow ends.[6,46,47]

DISCUSSION

We developed a reference-free platform containing a built-in, implied, zero-stress state that allows complete capture of cell-induced 3D material deformation and force profiles. The platform tracks material deformation as a function of centroid displacement of photolithographically patterned fluorescent fiducial markers embedded in a base hydrogel. The ability to capture both the reference state and displaced state in a single image stack greatly facilitates data collection allowing for a large cell population to be analyzed in a single experiment, thereby increasing throughput. It is important to note that circumventing the need for a reference image is not a new concept. A number of platforms exist that contain a built-in reference state achieved through implementing regular arrays

DOI: 10.1021/acsami.9b04362
ACS Appl. Mater. Interfaces 2019, 11, 18233–18241

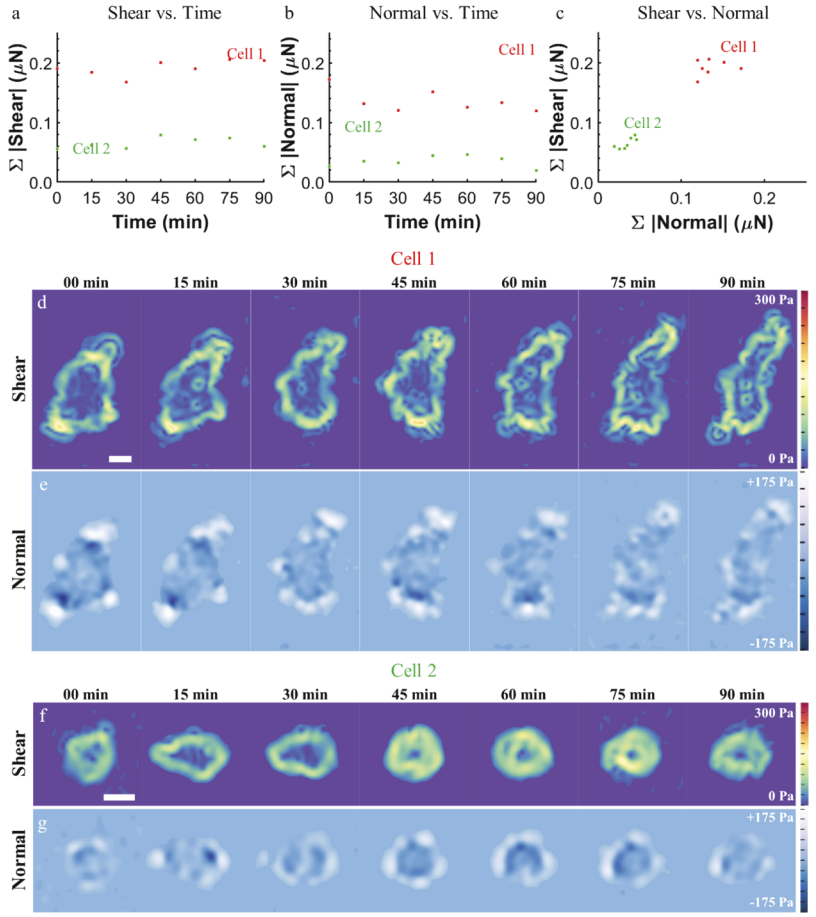

Figure 6. Time-lapse, cell-induced hydrogel traction measurements. The sum of (a) shear and (b) normal components of traction for a well-spread cell (cell 1) and a spreading cell (cell 2) over 90 min at 15 min intervals. (c) Although shear and normal traction magnitudes vary with time, their magnitudes are linearly correlated at all time points. Heatmaps of (d,f) shear stress and (e,g) normal stress for cell 1 and cell 2. SB = 20 μm. See Movies S1 and S2.

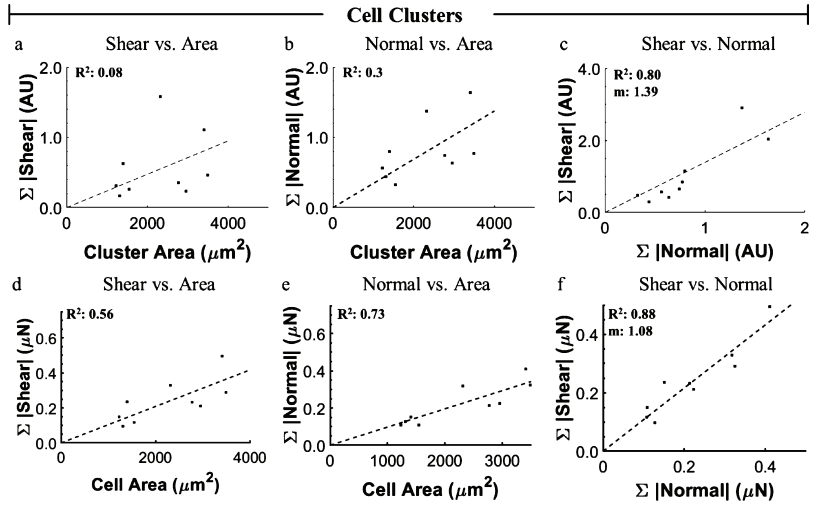

Figure 7. Magnitudes and distributions of cell cluster-induced hydrogel deformations and forces. Cell clusters (n = 9) displayed similar trends between (a) shear and (b) normal deformation with spread area, as well as (c) shear vs normal, that was observed for individual cells. (a,b) are normalized to the highest value measured in the individual, single-cell data in the respective category (i.e., shear or normal). Shear and normal data in (c) are normalized to the highest normal deformation measured in individual cells. (d–f) Calculated forces corresponding to (a–c), respectively.

of fiducial markers.[26,28,29,48−51] To achieve reference-free functionality, this platform uses a new approach to approximate the zero-stress state positions of fiducial markers. Developing the methodology to analyze displacements in this platform required characterizing the precision of the laser scanning microscope used for multiphoton chemical coupling. To minimize error, patterning dimensions that had the most consistent and predictable spacing of rows of markers were

DOI: 10.1021/acsami.9b04362
ACS Appl. Mater. Interfaces 2019, 11, 18233−18241

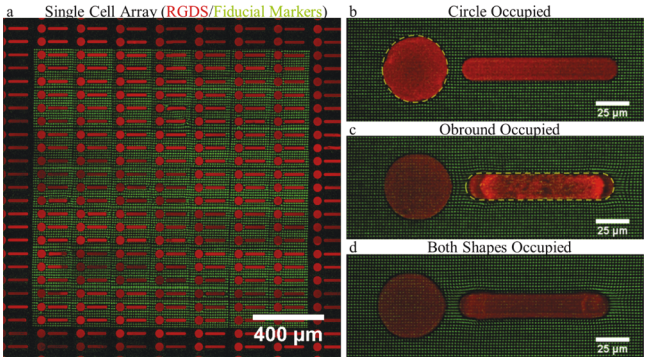

Figure 8. Fabrication of single-cell pattern arrays. (a) Fluorescent image of an array of circle and obround patterns composed of an (red) acrylated RGDS peptide on top of (green) TFM fiducial markers. (b–d) *Z*-projections of several permutations of ASCs adhered to patterns demonstrate that a variety of deformation profiles can be imposed on the cells using two-photon lithography to augment TFM studies.

identified and linear fits of individual rows in these dimensions were used to determine reference locations of displaced markers (see the Supporting Information). Linear fits of columns through the *Z*-dimension accurately predict *X* and *Y* reference positions, and similarly, linear fits of rows through the *X*-dimension accurately predict *Y* and *Z* reference positions. The intersection of these two independent fits provides the 3D nonstressed, reference position for every marker in the data set.

As an example of this platform's potential applications, we measured the 3D deformation profiles induced by HUVECs. Cells generate both in-plane and out-of-plane traction components, inducing 3D deformation in the underlying material. The spatial distribution, relative magnitude, and temporal linking suggest that both the in-plane and out-of-plane deformation are linked and may be a direct or indirect product of myosin-mediated cell contractility. On the basis of the distribution of normal material deformations beneath adherent cells, we expect that normal deformation may be, at least in part, the result of the cellular cortex pressing into the hydrogel perhaps because of the mechanisms described previously in *Dictyostelium* cells.[12] However, we discovered that normal deformation was most commonly either near or coincident with large shear deformation, which may also suggest that some component of normal deformation is simply the material response of the hydrogel to a high-magnitude shear. This is reinforced by the cell cluster data, where the spatial distribution of measured deformation did not follow the same pattern as individual cells (Figure S2), although the linear relationship between shear and normal deformation and forces held. Although it is clear that cells are responsible for generating normal force, it is unclear how it may be translated into the cell and what role, if any, this force plays in determining cell behavior. However, recent studies have shown that adhesion sites under the nucleus are compressed[52] and that force applied to the nucleus results in nuclear deformation and chromatin remodeling which can impact cell fate.[14,15,20,21] We also presented material displacement data converted to tractions. Several strategies exist for this conversion that are applicable to the workflow presented here; the method we used was found to be most compatible with our existing code.[18,38] Regardless of the methodology used to convert these data, other studies suggest that describing cellular tension in terms of material displacement yield useful information on their own.[17,53]

Although the ubiquitous RGDS ligand was used in this study, essentially any desired peptide or protein which can be functionalized with a compatible acrylate-PEG linker can be coupled to or patterned on the surface in a similar manner. In this way, the platform affords control over cell area, shape, focal adhesion distribution, and other physical aspects which have demonstrated roles in mechanotransduction pathways. In addition, digital masks, rather than physical masters, are used to control pattern geometry allowing new and interesting patterns to be implemented quickly.[54−59]

Traction forces have recently been used to distinguish the response between diseased and normal airway smooth muscle cells to bronchoconstrictor drugs in a high-throughput manner, demonstrating the potential of cellular traction as a metric for drug screening applications.[17] Also, another reference-free approach recently demonstrated the ability to simultaneously measure cell-generated tractions and the phosphorylation state of paxillin by combining TFM with traditional immunofluorescence labeling.[26,30] Similar applications may be possible with the TFM platform described here which could potentially aid throughput of such investigations.

There are a couple of considerations to keep in mind when determining the proper marker spacing when using this platform which include the level of tension generated by the cells being measured and the hydrogel elasticity. The fluorescent markers are composed of the same material as the base hydrogel and therefore deform with the base hydrogel in response to cellular tractions. If spaced too close to each other, the markers may begin to overlap in cases of high substrate deformation, making accurate centroid detection difficult. This can be avoided by either increasing the marker spacing or increasing the hydrogel elasticity. Increasing marker spacing lowers resolution while increasing hydrogel elasticity leads to lower deformations. For the cell types used here, HUVECs and ASCs, cultured on a 4 kPa hydrogel, we determined that a 2.12 μm spacing in *X*,*Y* provided enough spacing to avoid marker overlap while providing sufficient resolution to describe the traction profiles. An approach to decrease marker spacing includes the incorporation of additional marker colors which has been implemented in bead-based and reference-free TFM platforms to increase resolution.[24,26]

With regard to fabrication time, although multiphoton lithography provides high-resolution, 3D control over photoinitiation events, it is a serial process limited by the speed in which photocoupling occurs. In this study, a write speed of 1.25 $mm^2\ h^{-1}$ was achieved and has since been improved to 1.9 $mm^2\ h^{-1}$ using a piezo-actuated *z*-axis stage controller. This current write speed allows fabrication of a 2.2 mm^2 array of fiducial markers that extends 30 μm into the hydrogel, from the surface (nine layers of markers spaced at 3.5 μm) in 70 min.

CONCLUSIONS

In summary, a new TFM platform was developed that offers complete control over 3D fiducial marker placement to simplify measurement of cell-induced normal and shear material deformation in individual cells, cell clusters, and patterned cells.

DOI: 10.1021/acsami.9b04362
ACS Appl. Mater. Interfaces 2019, 11, 18233−18241

■ ASSOCIATED CONTENT

Supporting Information

The Supporting Information is available free of charge on the ACS Publications website at DOI: 10.1021/acsami.9b04362.

Sample accuracy histograms; example brightfield images and deformation heatmaps of cell clusters; and materials and methods (PDF)

Time-lapse movie of cell 1 shown in Figure 6 (MP4)

Time-lapse movie of cell 2 shown in Figure 6 (MP4)

■ AUTHOR INFORMATION

Corresponding Author

*E-mail: jhslater@udel.edu.

ORCID

John H. Slater: 0000-0002-2453-6665

Notes

The authors declare no competing financial interest.

■ ACKNOWLEDGMENTS

O.A.B. was supported by funding from a NSF IGERT SBE2 fellowship (1144726), startup funds provided by the University of Delaware, and the National Institutes of Health/National Cancer Institute IMAT Program (R21CA214299). J.H.S. is supported by funding from the National Institutes of Health/National Cancer Institute IMAT Program (R21CA214299) and the National Science Foundation CAREER Award Program (1751797). Microscopy access was supported by grants from the NIH-NIGMS (P20 GM103446), the NSF (IIA-1301765), and the State of Delaware. The structured illumination microscope was acquired with funds from the State of Delaware Federal Research and Development Grant Program (16A00471). The LSM880 confocal microscope used for TP-LSL was acquired with a shared instrumentation grant (S10 OD016361).

■ REFERENCES

(1) Rauskolb, C.; Sun, S.; Sun, G.; Pan, Y.; Irvine, K. D. Cytoskeletal Tension Inhibits Hippo Signaling through an Ajuba-Warts Complex. *Cell* **2014**, *158*, 143−156.

(2) Huang, S.; Chen, C. S.; Ingber, D. E. Control of Cyclin D1, P27Kip1, and Cell Cycle Progression in Human Capillary Endothelial Cells by Cell Shape and Cytoskeletal Tension. *Mol. Biol. Cell* **1998**, *9*, 3179−3193.

(3) Provenzano, P. P.; Keely, P. J. Mechanical Signaling through the Cytoskeleton Regulates Cell Proliferation by Coordinated Focal Adhesion and Rho GTPase Signaling. *J. Cell Sci.* **2011**, *124*, 1195−1205.

(4) Reilly, G. C.; Engler, A. J. Intrinsic Extracellular Matrix Properties Regulate Stem Cell Differentiation. *J. Biomech.* **2010**, *43*, 55−62.

(5) Wen, J. H.; Vincent, L. G.; Fuhrmann, A.; Choi, Y. S.; Hribar, K. C.; Taylor-Weiner, H.; Chen, S.; Engler, A. J. Interplay of Matrix Stiffness and Protein Tethering in Stem Cell Differentiation. *Nat. Mater.* **2014**, *13*, 979−987.

(6) Lee, J.; Abdeen, A. A.; Tang, X.; Saif, T. A.; Kilian, K. A. Geometric Guidance of Integrin Mediated Traction Stress during Stem Cell Differentiation. *Biomaterials* **2015**, *69*, 174−183.

(7) Steward, A. J.; Kelly, D. J. Mechanical Regulation of Mesenchymal Stem Cell Differentiation. *J. Anat.* **2015**, *227*, 717−731.

(8) Lv, H.; Li, L.; Sun, M.; Zhang, Y.; Chen, L.; Rong, Y.; Li, Y. Mechanism of Regulation of Stem Cell Differentiation by Matrix Stiffness. *Stem Cell Res. Ther.* **2015**, *6*, 103.

(9) Tijore, A.; Cai, P.; Nai, M. H.; Zhuyun, L.; Yu, W.; Tay, C. Y.; Lim, C. T.; Chen, X.; Tan, L. P. Role of Cytoskeletal Tension in the Induction of Cardiomyogenic Differentiation in Micropatterned Human Mesenchymal Stem Cell. *Adv. Healthcare Mater.* **2015**, *4*, 1399−1407.

(10) Lombardi, M. L.; Knecht, D. A.; Dembo, M.; Lee, J. Traction Force Microscopy in Dictyostelium Reveals Distinct Roles for Myosin II Motor and Actin-Crosslinking Activity in Polarized Cell Movement. *J. Cell Sci.* **2007**, *120*, 1624−1634.

(11) Plotnikov, S. V.; Pasapera, A. M.; Sabass, B.; Waterman, C. M. Force Fluctuations within Focal Adhesions Mediate ECM-Rigidity Sensing to Guide Directed Cell Migration. *Cell* **2012**, *151*, 1513−1527.

(12) Álvarez-González, B.; Meili, R.; Bastounis, E.; Firtel, R. A.; Lasheras, J. C.; del Álamo, J. C. Three-Dimensional Balance of Cortical Tension and Axial Contractility Enables Fast Amoeboid Migration. *Biophys. J.* **2015**, *108*, 821−832.

(13) Kim, K.; Kim, K.; Ryu, J. H.; Lee, H. Chitosan-catechol: A polymer with long-lasting mucoadhesive properties. *Biomaterials* **2015**, *52*, 161−170.

(14) Versaevel, M.; Grevesse, T.; Gabriele, S. Spatial Coordination between Cell and Nuclear Shape within Micropatterned Endothelial Cells. *Nat. Commun.* **2012**, *3*, 671.

(15) Buxboim, A.; Irianto, J.; Swift, J.; Athirasala, A.; Shin, J.-W.; Rehfeldt, F.; Discher, D. E. Coordinated Increase of Nuclear Tension and Lamin-A with Matrix Stiffness Outcompetes Lamin-B Receptor That Favors Soft Tissue Phenotypes. *Mol. Biol. Cell* **2017**, *28*, 3333−3348.

(16) Li, Q.; Makhija, E.; Hameed, F. M.; Shivashankar, G. V. Micropillar Displacements by Cell Traction Forces Are Mechanically Correlated with Nuclear Dynamics. *Biochem. Biophys. Res. Commun.* **2015**, *461*, 372−377.

(17) Pushkarsky, I.; Tseng, P.; Black, D.; France, B.; Warfe, L.; Koziol-White, C. J.; Jester, W. F.; Trinh, R. K.; Lin, J.; Scumpia, P. O.; Morrison, S. L.; Panettieri, R. A.; Damoiseaux, R.; Di Carlo, D. Elastomeric Sensor Surfaces for High-Throughput Single-Cell Force Cytometry. *Nat. Biomed. Eng.* **2018**, *2*, 124−137.

(18) Legant, W. R.; Choi, C. K.; Miller, J. S.; Shao, L.; Gao, L.; Betzig, E.; Chen, C. S. Multidimensional Traction Force Microscopy Reveals Out-of-Plane Rotational Moments about Focal Adhesions. *Proc. Natl. Acad. Sci. U.S.A.* **2013**, *110*, 881−886.

(19) Yeh, Y.-T.; Serrano, R.; François, J.; Chiu, J.-J.; Li, Y.-S. J.; del Álamo, J. C.; Chien, S.; Lasheras, J. C. Three-Dimensional Forces Exerted by Leukocytes and Vascular Endothelial Cells Dynamically Facilitate Diapedesis. *Proc. Natl. Acad. Sci. U.S.A.* **2018**, *115*, 133−138.

(20) Cho, S.; Irianto, J.; Discher, D. E. Mechanosensing by the Nucleus: From Pathways to Scaling Relationships. *J. Cell Biol.* **2017**, *216*, 305−315.

(21) Wang, Y.; Nagarajan, M.; Uhler, C.; Shivashankar, G. V. Orientation and repositioning of chromosomes correlate with cell geometry-dependent gene expression. *Mol. Biol. Cell* **2017**, *28*, 1997−2009.

(22) Sabass, B.; Gardel, M. L.; Waterman, C. M.; Schwarz, U. S. High Resolution Traction Force Microscopy Based on Experimental and Computational Advances. *Biophys. J.* **2008**, *94*, 207−220.

(23) Munevar, S.; Wang, Y.-l.; Dembo, M. Traction Force Microscopy of Migrating Normal and H-Ras Transformed 3T3 Fibroblasts. *Biophys. J.* **2001**, *80*, 1744−1757.

(24) Colin-York, H.; Shrestha, D.; Felce, J. H.; Waithe, D.; Moeendarbary, E.; Davis, S. J.; Eggeling, C.; Fritzsche, M. Super-Resolved Traction Force Microscopy (STFM). *Nano Lett.* **2016**, *16*, 2633−2638.

(25) Colin-York, H.; Fritzsche, M. The Future of Traction Force Microscopy. *Curr. Opin. Biomed. Eng.* **2018**, *5*, 1−5.

(26) Bergert, M.; Lendenmann, T.; Zündel, M.; Ehret, A. E.; Panozzo, D.; Richner, P.; Kim, D. K.; Kress, S. J. P.; Norris, D. J.; Sorkine-Hornung, O.; Mazza, E.; Poulikakos, D.; Ferrari, A. Confocal Reference Free Traction Force Microscopy. *Nat. Commun.* **2016**, *7*, 12814.

DOI: 10.1021/acsami.9b04362
ACS Appl. Mater. Interfaces 2019, 11, 18233−18241

(27) Schwarz, U. S.; Balaban, N. Q.; Riveline, D.; Addadi, L.; Bershadsky, A.; Safran, S. A.; Geiger, B. Measurement of Cellular Forces at Focal Adhesions Using Elastic Micro-Patterned Substrates. *Mater. Sci. Eng., C* **2003**, *23*, 387−394.
(28) Tan, J. L.; Tien, J.; Pirone, D. M.; Gray, D. S.; Bhadriraju, K.; Chen, C. S. Cells Lying on a Bed of Microneedles: An Approach to Isolate Mechanical Force. *Proc. Natl. Acad. Sci. U.S.A.* **2003**, *100*, 1484−1489.
(29) Desai, R. A.; Yang, M. T.; Sniadecki, N. J.; Legant, W. R.; Chen, C. S. Microfabricated Post-Array-Detectors (MPADs): An Approach to Isolate Mechanical Forces. *J. Visualized Exp.* **2007**, *7*, 311.
(30) Panagiotakopoulou, M.; Lendenmann, T.; Pramotton, F. M.; Giampietro, C.; Stefopoulos, G.; Poulikakos, D.; Ferrari, A. Cell Cycle-Dependent Force Transmission in Cancer Cells. *Mol. Biol. Cell* **2018**, *29*, 2528−2539.
(31) Culver, J. C.; Hoffmann, J. C.; Poché, R. A.; Slater, J. H.; West, J. L.; Dickinson, M. E. Three-Dimensional Biomimetic Patterning in Hydrogels to Guide Cellular Organization. *Adv. Mater.* **2012**, *24*, 2344−2348.
(32) Hahn, M. S.; Miller, J. S.; West, J. L. Three-Dimensional Biochemical and Biomechanical Patterning of Hydrogels for Guiding Cell Behavior. *Adv. Mater.* **2006**, *18*, 2679−2684.
(33) Wylie, R. G.; Ahsan, S.; Aizawa, Y.; Maxwell, K. L.; Morshead, C. M.; Shoichet, M. S. Spatially Controlled Simultaneous Patterning of Multiple Growth Factors in Three-Dimensional Hydrogels. *Nat. Mater.* **2011**, *10*, 799−806.
(34) Wylie, R. G.; Shoichet, M. S. Three-Dimensional Spatial Patterning of Proteins in Hydrogels. *Biomacromolecules* **2011**, *12*, 3789−3796.
(35) Wosnick, J. H.; Shoichet, M. S. Three-Dimensional Chemical Patterning of Transparent Hydrogels. *Chem. Mater.* **2008**, *20*, 55−60.
(36) Luo, Y.; Shoichet, M. S. A Photolabile Hydrogel for Guided Three-Dimensional Cell Growth and Migration. *Nat. Mater.* **2004**, *3*, 249−253.
(37) Reinhart-King, C. A.; Dembo, M.; Hammer, D. A. Endothelial Cell Traction Forces on RGD-Derivatized Polyacrylamide Substrata. *Langmuir* **2003**, *19*, 1573−1579.
(38) Toyjanova, J.; Bar-Kochba, E.; López-Fagundo, C.; Reichner, J.; Hoffman-Kim, D.; Franck, C. High Resolution, Large Deformation 3D Traction Force Microscopy. *PLoS One* **2014**, *9*, No. e90976.
(39) Kalcioglu, Z. I.; Mahmoodian, R.; Hu, Y.; Suo, Z.; Van Vliet, K. J. From Macro- to Microscale Poroelastic Characterization of Polymeric Hydrogels via Indentation. *Soft Matter* **2012**, *8*, 3393.
(40) Wang, M.; Hill, R. J. Electric-Field-Induced Displacement of Charged Spherical Colloids in Compressible Hydrogels. *Soft Matter* **2008**, *4*, 1048.
(41) Kloxin, A. M.; Kloxin, C. J.; Bowman, C. N.; Anseth, K. S. Mechanical Properties of Cellularly Responsive Hydrogels and Their Experimental Determination. *Adv. Mater.* **2010**, *22*, 3484−3494.
(42) Franck, C.; Maskarinec, S. A.; Tirrell, D. A.; Ravichandran, G. Three-Dimensional Traction Force Microscopy: A New Tool for Quantifying Cell-Matrix Interactions. *PLoS One* **2011**, *6*, No. e17833.
(43) Maruthamuthu, V.; Sabass, B.; Schwarz, U. S.; Gardel, M. L. Cell-ECM Traction Force Modulates Endogenous Tension at Cell-Cell Contacts. *Proc. Natl. Acad. Sci. U.S.A.* **2011**, *108*, 4708−4713.
(44) Ng, M. R.; Besser, A.; Brugge, J. S.; Danuser, G. Mapping the Dynamics of Force Transduction at Cell−cell Junctions of Epithelial Clusters. *eLife* **2014**, *3*, No. e03282.
(45) Mertz, A. F.; Che, Y.; Banerjee, S.; Goldstein, J. M.; Rosowski, K. A.; Revilla, S. F.; Niessen, C. M.; Marchetti, M. C.; Dufresne, E. R.; Horsley, V. Cadherin-Based Intercellular Adhesions Organize Epithelial Cell-Matrix Traction Forces. *Proc. Natl. Acad. Sci. U.S.A.* **2013**, *110*, 842−847.
(46) Oakes, P. W.; Banerjee, S.; Marchetti, M. C.; Gardel, M. L. Geometry Regulates Traction Stresses in Adherent Cells. *Biophys. J.* **2014**, *107*, 825−833.
(47) Rape, A. D.; Guo, W.-h.; Wang, Y.-l. The Regulation of Traction Force in Relation to Cell Shape and Focal Adhesions. *Biomaterials* **2011**, *32*, 2043−2051.
(48) Tong, M. H.; Huang, N.; Zhang, W.; Zhou, Z. L.; Ngan, A. H. W.; Du, Y.; Chan, B. P. Multiphoton Photochemical Crosslinking-Based Fabrication of Protein Micropatterns with Controllable Mechanical Properties for Single Cell Traction Force Measurements. *Sci. Rep.* **2016**, *6*, 20063.
(49) Spivey, E. C.; Ritschdorff, E. T.; Connell, J. L.; McLennon, C. A.; Schmidt, C. E.; Shear, J. B. Multiphoton Lithography of Unconstrained Three-Dimensional Protein Microstructures. *Adv. Funct. Mater.* **2013**, *23*, 333−339.
(50) Fu, J.; Wang, Y.-K.; Yang, M. T.; Desai, R. A.; Yu, X.; Liu, Z.; Chen, C. S. Mechanical Regulation of Cell Function with Geometrically Modulated Elastomeric Substrates. *Nat. Methods* **2010**, *7*, 733−736.
(51) Shiu, J.-Y.; Aires, L.; Lin, Z.; Vogel, V. Nanopillar Force Measurements Reveal Actin-Cap-Mediated YAP Mechanotransduction. *Nat. Cell Biol.* **2018**, *20*, 262−271.
(52) Rothenberg, K. E.; Neibart, S. S.; LaCroix, A. S.; Hoffman, B. D. Controlling Cell Geometry Affects the Spatial Distribution of Load Across Vinculin. *Cell. Mol. Bioeng.* **2015**, *8*, 364−382.
(53) Stout, D. A.; Bar-Kochba, E.; Estrada, J. B.; Toyjanova, J.; Kesari, H.; Reichner, J. S.; Franck, C. Mean deformation metrics for quantifying 3D cell-matrix interactions without requiring information about matrix material properties. *Proc. Natl. Acad. Sci. U.S.A.* **2016**, *113*, 2898−2903.
(54) Slater, J. H.; Miller, J. S.; Yu, S. S.; West, J. L. Fabrication of Multifaceted Micropatterned Surfaces with Laser Scanning Lithography. *Adv. Funct. Mater.* **2011**, *21*, 2876−2888.
(55) Slater, J. H.; Culver, J. C.; Long, B. L.; Hu, C. W.; Hu, J.; Birk, T. F.; Qutub, A. A.; Dickinson, M. E.; West, J. L. Recapitulation and Modulation of the Cellular Architecture of a User-Chosen Cell of Interest Using Cell-Derived, Biomimetic Patterning. *ACS Nano* **2015**, *9*, 6128−6138.
(56) Slater, J. H.; West, J. L. *Fabrication of Multifaceted, Micropatterned Surfaces and Image-Guided Patterning Using Laser Scanning Lithography*, 1st ed.; Elsevier Inc., 2014; Vol. *119*.
(57) Heintz, K. A.; Mayerich, D.; Slater, J. H. Image-Guided, Laser-Based Fabrication of Vascular-Derived Microfluidic Networks. *J. Visualized Exp.* **2017**, *119*, 1−10.
(58) Heintz, K. A.; Bregenzer, M. E.; Mantle, J. L.; Lee, K. H.; West, J. L.; Slater, J. H. Fabrication of 3D Biomimetic Microfluidic Networks in Hydrogels. *Adv. Healthcare Mater.* **2016**, *5*, 2153−2160.
(59) Shukla, A.; Slater, J. H.; Culver, J. C.; Dickinson, M. E.; West, J. L. Biomimetic Surface Patterning Promotes Mesenchymal Stem Cell Differentiation. *ACS Appl. Mater. Interfaces* **2016**, *8*, 21883−21892.

DOI: 10.1021/acsami.9b04362
ACS Appl. Mater. Interfaces 2019, 11, 18233−18241

Supporting Information

A Reference-Free Traction Force Microscopy Platform Fabricated via Two-Photon Laser Scanning Lithography Enables Facile Measurement of Cell-Generated Forces

*Omar A. Banda, Chandran R. Sabanayagam, John H. Slater**

*Corresponding Author; Email: jhslater@udel.edu

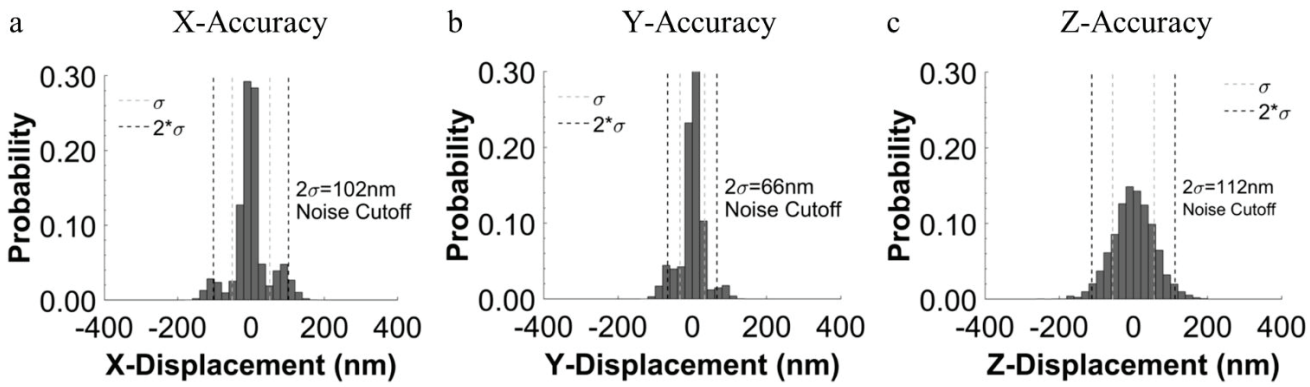

Figure S1. Quantifying the accuracy of the implied reference. (a,b,c) Histograms displaying the accuracy of reference lines for each cardinal direction, shown as the probability of locating marker centroids in a non-stressed array. The darker dashed vertical lines indicate two standard deviations from the mean and this value was used to set the lower limit for displacement measurements. Accuracy in each direction varies due to the different modes of stepping used during patterning. (n = 2,651 markers tracked for each direction). See main manuscript text for average over many volumes.

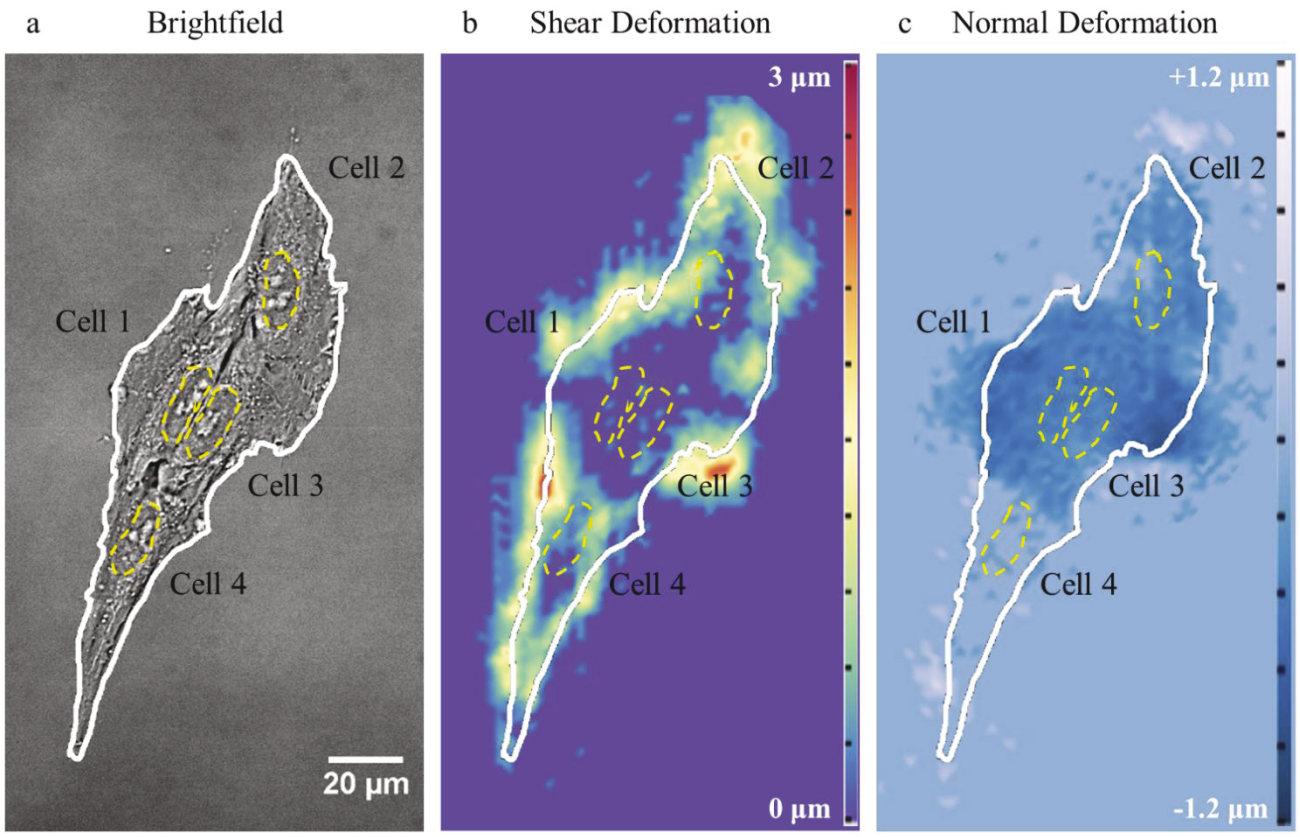

Figure S2. Material deformation induced by a cell cluster. (a) Brightfield image of a cluster of four HUVECs given arbitrary number assignments. The nucleus of each cell is outlined with a dashed yellow line. (b) Shear deformation induced by the cell cluster. (c) Normal deformation induced by the cell cluster. While the spatial distribution of shear and normal deformation in cell clusters does not match individual cells, the ratio of shear to normal still holds. For example, cell number 4 generates minimal normal deformation, despite generating large shear deformation.

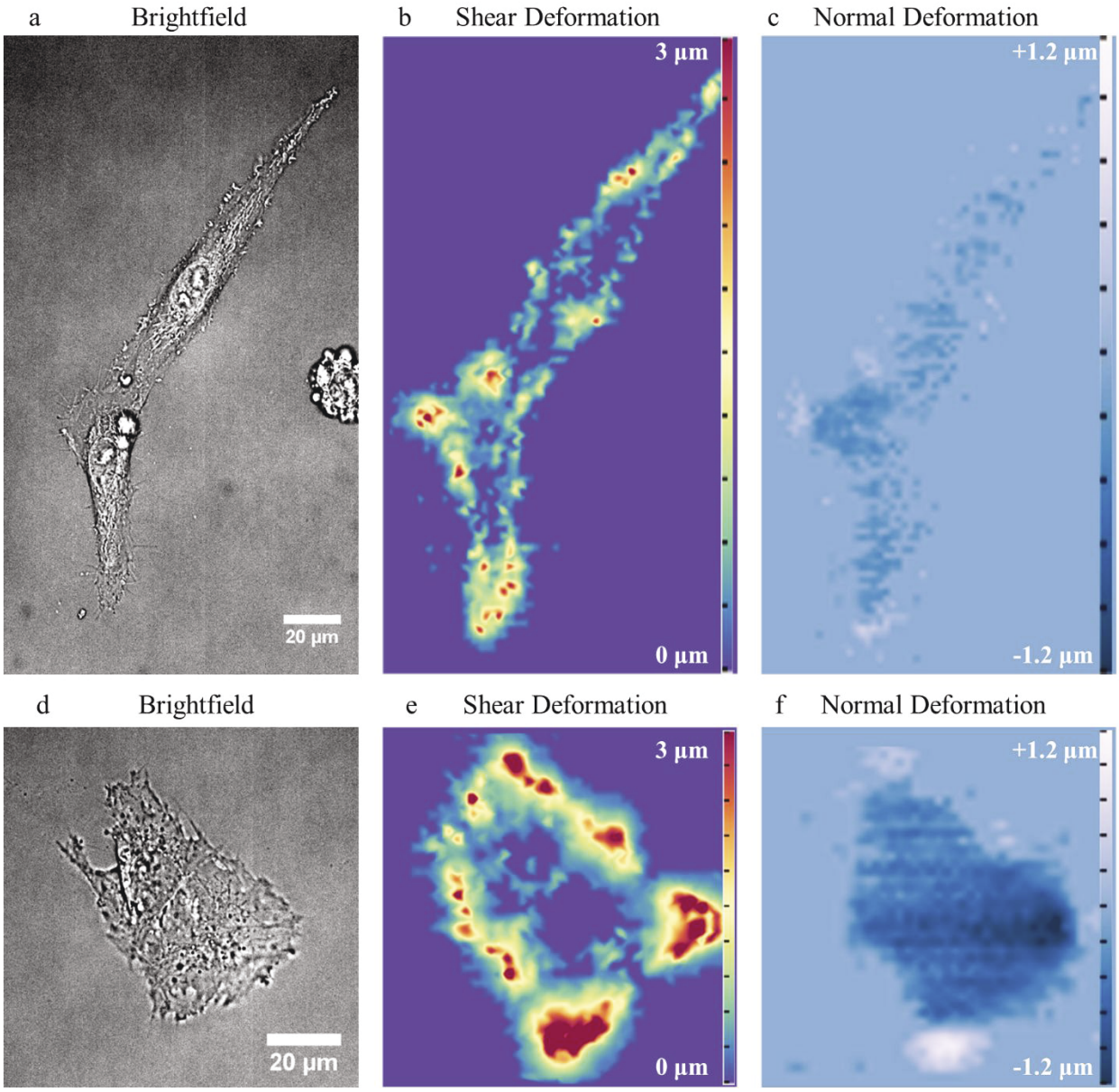

Figure S3. Material deformation induced by cell clusters. (a,d) Brightfield images of clusters of 2 HUVECs. (b,e) Shear deformation induced by the cell clusters. (c,f) Normal deformation induced by the cell clusters.

Video S1. Time-lapse of a spread HUVEC. Shown are (a) transmitted and (b) z-projected fluorescence images of a spread HUVEC captured at 15 min intervals over 90 min. The interpolated displacement fields of (c) shear and (d) normal deformation measured from the fluorescent image stack.

Video S2. Time-lapse of a spreading HUVEC. Shown are (a) transmitted and (b) z-projected fluorescence images of a spread HUVEC captured at 15 min intervals over 90 min. The interpolated displacement fields of (c) shear and (d) normal deformation measured from the fluorescent image stack.

Materials & Methods

All materials were purchased from Sigma-Aldrich (Sigma-Aldrich, St. Louis, MO) unless otherwise specified.

Cell Culture

Human Umbilical Vein Endothelial Cells (HUVECs, Lonza, Catalog No. C2519A) were cultured in EGM-2 media (Clonetics™ EGM™-2 BulletKit™; Lonza Catalog No. CC-3162; 500 ml of EBM™-2 Medium and the following supplements: human Epidermal Growth Factor (hEGF), 0.5 ml; Vascular Endothelial Growth Factor (VEGF), 0.5 ml; R3-Insulin-like Growth Factor-1 (R3-IGF-1), 0.5 ml; Ascorbic Acid, 0.5 ml; Hydrocortisone, 0.2 ml; human Fibroblast Growth Factor-Beta (hFGF-β), 2.0 ml; Heparin (0.5 ml); Fetal Bovine Serum (FBS), 10.0 ml; Gentamicin/Amphotericin-B (GA), 0.5 ml) during expansion and traction force microscopy (TFM) experiments. HUVECs were cultured at 37 °C and 5% CO_2 and the media was changed every two days. HUVECs were passaged at ~80% confluency and cultured on TFM hydrogels at passage 7 for all experiments.

ASC52telo, hTERT immortalized adipose-derived mesenchymal stem cells (ATCC® SCRC-4000™) (ASCs) were cultured in mesenchymal stem cell growth medium (ATCC Catalog No. PCS-500-040, PCS-500-30) containing 482 mL of basal medium, 10mL of MSC supplement (2% FBS, 5 ng/mL rh FGF basic, 5 ng/mL rh FGF acidic, 5 ng/mL rh EGF), 6mL of L-Alanyl-L-Glutamine (2.4mM, final concentration) and 2 mL of 50mg/ml G418 (0.2mg/mL, final concentration), and passaged at ~80% confluency.

Synthesis of PEGDA

PEGDA (3.4kDa) was synthesized as previously described[1,2]. Briefly, poly(ethylene glycol) (3.4kDa; Cat.# 202444-500G) was reacted with acryloyl chloride (AC; Cat.#549797-5G) in the presence of triethylamine (TEA; Cat.#471283-500ML) in anhydrous dichloromethane (DCM; Cat.#270997-100ML) at molar ratios of 4:1 (AC:PEG) and 2:1 (TEA:PEG) overnight under argon. The result was mixed vigorously with an aqueous K_2CO_3 (Cat. #791776) solution and allowed to reach a visible phase-separation over 24 hrs. $MgSO_4$ (Cat. #M7506) was added to the organic phase to remove any remaining aqueous contaminants. The purified organic solution containing PEGDA was distilled through rotary evaporation to remove excess DCM. PEGDA was precipitated from the remaining DCM in cold diethyl ether, isolated through vacuum filtration, and thoroughly dried. The final PEGDA product was analyzed via ^{1}H-NMR to confirm substitution of terminal hydroxyls for acrylates.

Synthesis of Acrylated-PEG Derivatives

To synthesize acrylate-PEG-RGDS, a hetero-bifunctional PEG with a chain-end acrylate and succinimidyl-ester (PEG-SVA; Laysan Bio; Arab, AL; Cat. # ACRL-PEG-SVA-3400-500mg) was reacted with the amine terminus of the peptide sequence RGDS (GenScript; Piscataway, NJ; Cat.# RP10861) in the presence of diisopropylethylamine (Cat.# D125806) in DMSO (Cat.# 276855) for 24 hrs. The product was dialyzed against ultrapure water with 4 exchanges at least 2 hrs apart over 2 days. The aqueous product was frozen at -20 °C for 24 hrs, -80 °C for 4 hrs, and lyophilized for 2 days at -85 °C at 0.120 mbar followed by analysis via gel permeation chromatography in ultrapure water to estimate purity (>90% Acryl-PEG-RGDS). Fluorophore-labeled PEG acrylate was synthesized in a two-step reaction through similar NHS-chemistry. First, diamine-PEG (Laysan Bio; Cat.# NH2-PEG-NH2-2K-1g) and either AlexaFluor488 (AF488), or AlexaFluor633 (AF633) succinimidyl ester (ThermoFisher; Cat.# A20000/A20005) were reacted at a molar ratio of 75:1 in DMSO in the presence of

diisopropylethylamine for 24 hrs. The resulting products were reacted with PEG-SVA (165:1, PEG-SVA:AlexaFluor dye) for 24 hrs. As before, the product was dialyzed and lyophilized. All PEG derivatives were stored at -80 °C under Argon until use.

Base Hydrogel Formulation and Photopolymerization

Base hydrogels were polymerized through a photo-initiated radical polymerization reaction. With sterile PBS (pH 7.4) as a solvent, hydrogel formulations were 5% mass-to-volume PEGDA, 10 mM PEG-RGDS, and were doped with 0.08% mass-to-volume AF488-labeled PEG-derivative to allow for visualization via fluorescence microscopy. The photo-initiator, lithium phenyl-2,4,6-trimethylbenzoylphosphinate (LAP), was synthesized as previously described[3]. Briefly, dimethyl phenylphosphonite was reacted with an equimolar amount of 2,4,6-trimethylbenzoyl chloride under argon for 24 hrs with stirring. A fourfold excess of lithium bromide in 100 ml of 2-butanone was added to the reaction and heated to 50 °C for 10 mins. The solution was cooled to room temperature over 4 hrs, vacuum filtered, and washed with 300 ml of 2-butanone. The product was dried in a fume hood, stored in an amber vial at 4 °C, and used at a concentration of 3 mg/ml. The hydrogels were photopolymerized under a broad spectrum UV lamp (UVP; Blak-Ray™ Model B-100AP/R lamp; ~12 mW at 370 nm) for 1 min between a thin smooth sheet of perfluoroalkoxy alkanes (PFA, McMaster Carr) and an methacrylate-silane functionalized glass coverslip. The coverslip-bound hydrogel was stored in sterile buffer.

Nano-Indentation Testing of Patterned and Non-Patterned Hydrogels

Operating under the assumption that PEGDA hydrogels are linear elastic materials, nanoindentation experiments were performed on the surface of the hydrogels in patterned and non-patterned areas. All indentations were performed using a Bruker BioScope Catalyst BioAFM indenter with a custom tip

comprising a 0.6 N m^{-1} Silicon Nitride cantilever and 45 μm diameter polystyrene spherical end. Indentation was performed at a rate of 2 μm s^{-1} to a trigger threshold of 72 nN. Force-indentation curves were collected for patterned (n=66 total curves from 3 regions) and non-patterned (n=63 curves from 3 regions) regions, and Young's modulus was approximated from fits of the retraction with force boundaries of 10-70% of the maximum using a spherical Hertzian model. All fits were performed in the NanoScope Analysis software package (v1.5).

Two-Photon Laser-Scanning Lithography for Fiducial Marker Patterning

A base hydrogel was assembled into a fluidic chamber (**Figure 1**) within a custom-designed and machined stage insert fitting the motorized stage on an upright Zeiss LSM 780 confocal microscope. A soaking solution (containing 5% mass/volume of the acryl-PEG-AF633, 1% volume/volume N-Vinylpyrrolidone, and 3 mg/ml LAP) was flowed into the soaking chamber containing the base hydrogel. An argon laser line (488nm) identified the AF488 signal in the base gel and was used to navigate to the center and surface of the hydrogel. Using a series of XZ tile scans, the surface of the hydrogel was leveled using set screws in the custom-built stage insert to improve spatial consistency of the pattern array relative to the surface. A Chameleon Vision 2 (Coherent Inc.; Santa Clara, CA) tuned to 740nm operating at a fluence of 3.7 nJ/μm^2 focused through a Zeiss C-Apochromat 40X 1.2 NA water-immersion objective was scanned at desired locations in the base hydrogel to initiate photo-polymerization of the fluorescently-labeled PEG monoacrylate. A digital mask containing single pixel features (~9.4 pixels/micron) was used to guide the position of the laser to specify pattern locations. The patterning scheme used contained a single row of 100 single pixel features with designated object spacing of 2.12 μm in the X-direction. Spacing in the Y- and Z-directions were controlled using the tile and z-stack functions respectively, in Zen software, and were specified as 2.12 μm in Y and 3.5 μm in Z. Patterning parameters were adjusted to reach a patterning speed of 1.25 mm^2 per hour. The resulting fiducial markers

resembled 3D Gaussian-like features with full-width, half-max dimensions of 0.84 ± 0.108 μm in XY and 3.73 ± 0.304 μm in Z.

Two-Photon Laser-Scanning Lithography for Patterning Adhesive Ligands

To incorporate the cell adhesive peptide, RGDS, a base hydrogel which did not contain acrylate PEG-RGDS was synthesized and patterned as described above. To add RGDS to the surface, PEG-RGDS was dissolved at a 10 mM concentration in the solution used for creating fiducial markers. This solution was soaked into the base hydrogel already decorated with fiducial markers. The hydrogel was allowed to reach a stable swelling point, and then TP-LSL was implemented using the same laser settings for creating fiducial markers to generate fluorescent adhesive regions.

Imaging Material Deformation During Cell Experiments

Before use, patterned hydrogels were rinsed in sterile PBS over 2 days with 4 exchanges of the sterile PBS wash solution. All fluorescent images of patterned features were captured using a Zeiss C-Apochromat 40X 1.2 NA water-immersion objective on a Zeiss AxioObserver Z1 microscope equipped with the Apotome2 structured illumination module and ORCA-Flash 4.0LT camera (Hamamatsu) with a 162.5 nm pixel size. Z-stacks were acquired at 0.4 μm intervals. Confocal quality images using the structured illumination were achieved using 3 phase images per captured view field. HUVECs or ASCs were seeded on patterned hydrogels at a density of ~ 40 cells/mm^2 in EGM-2 or MSC growth media, respectively. HUVECs were given at least 2 hrs to adhere before imaging. Time-lapse imaging was performed on the same Zeiss AxioObserver Z1 using a temperature-controlled enclosure set to 37 °C and 5% CO_2 with the sample on a heated stage insert set to 37 °C. Time-lapse brightfield and fluorescent images were acquired every 15 mins for 90 mins.

Measuring Cell-Induced Material Displacements

The following processing and analytical methods were performed using custom code written in Matlab, which may be accessed in an online public repository[4].

Image Processing: To reduce computational time in later steps, raw image stacks were cropped to regions containing a single cell or cell cluster and sufficient surrounding space to include non-stressed reference locations. Cropped image stacks of fluorescent markers were processed using a custom MatLab script (bpass3dMB.m; Maria Kilfoil 2005, based on Crocker and Grier 1991.[5–7]) which performs a 'mexican hat' wavelet convolution independently on all image axes using a one-dimensional kernel described by the vector:

$$\left[\left(\frac{e^{-\left(\frac{-r}{2N}\right)^2}}{S}+\frac{-1}{2r+1}\right),\left(\frac{e^{-\left(\frac{-r+1}{2N}\right)^2}}{S}+\frac{-1}{2r+1}\right),\ldots,\left(\frac{e^{-\left(\frac{r}{2N}\right)^2}}{S}+\frac{-1}{2r+1}\right)\right]$$

, where $S=\sum_{i=-r}^{r}\left(e^{-\left(\frac{i}{2N}\right)^2}\right)$, r is an integer describing a pixel length slightly larger than the expected radius in the respective dimension of a feature, and N describes the characteristic length scale of noise in the data in that same dimension.

2D Object Detection: Subpixel XY localizations of marker centroids in each plane within a Z-stack were detected using custom Matlab scripts (feature2D.m, localmax.m, rsqd.m, fracshift.m; Maria Kilfoil 2003, based on IDL code by John C. Crocker 1993 and David G. Grier 1992.[5–7]), which are based on finding a local intensity maxima in each 2D image and contains features including a minimum separation distance and a minimum intensity value to qualify as a detection. Subpixel localization is accomplished by approximating a center of mass (intensity) from an interpolated subarray centered around each detection with subarray dimensions related to the approximate expected radius of detections (**Figure S4**).

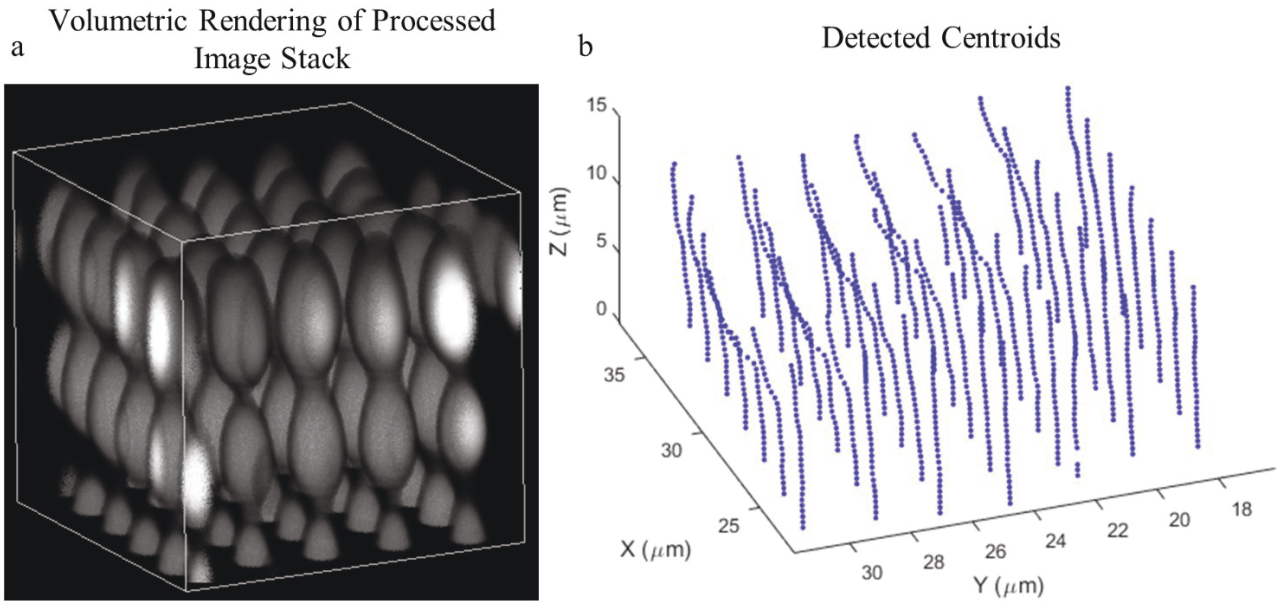

Figure S4. Two-dimensional object detection. (a) A volumetric rendering of a small volume of a processed image stack. (b) A centerline is traced through the long dimension (Z-direction) of the ellipsoids in the volumetric rendering. Detecting centroid locations on the center line, frame by frame in Z, is the first step in measuring deformation.

2D Object Linking through the Z-Dimension (Columns): Before measuring fluorescent marker shear displacement, detected objects were linked through the Z-dimension using custom particle tracking Matlab scripts (trackmem.m[7]) (**Figure S5**). The algorithm groups objects frame-by-frame through an overall minimization of object displacements. Errors in grouping were manually corrected using a custom Matlab script coding for an interactive user interface that provides the user with traces of grouped objects overlaying a Z-projection image as a visual-aid. Errors in automatic linking typically occurred in locations of large deformations and were relatively few (<< 1%)**.**

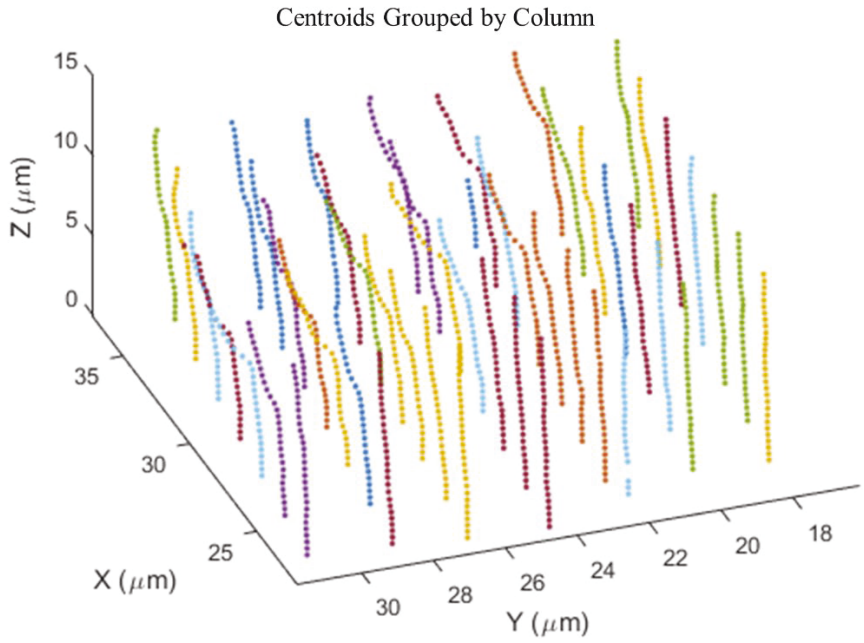

Figure S5. Linking detected centroids through the Z-direction. Detected centroids are grouped into columns using particle tracking analysis.

Approximating XY Reference Locations to Measure Shear Deformation: The assumption required for making measures of deformation in the XY plane was that detections which are sufficiently below the surface of the hydrogel were representative of the XY positions of non-deformed detections near the surface (**Figure S6a**). This assumption held true for the vast majority of cases after reaching depths of ~10-12 μm from the hydrogel surface (it should be noted that at this depth, deformations normal to the surface can often still be detected). The orientation of the 3D arrays within the hydrogels were not always perfectly level with the surface. This was accounted for by the inclusion of an algorithm to predict the contribution of tilt to the measured displacements as a function of depth, and the predicted contribution was subtracted from final displacement measures (Figure S6b). Briefly, for each displacement measure, the algorithm searched for the nearest non-deformed columns of detections. The average linear fit of the

non-deformed columns was used to determine the appropriate correction factor for each measure of displacement based on its depth.

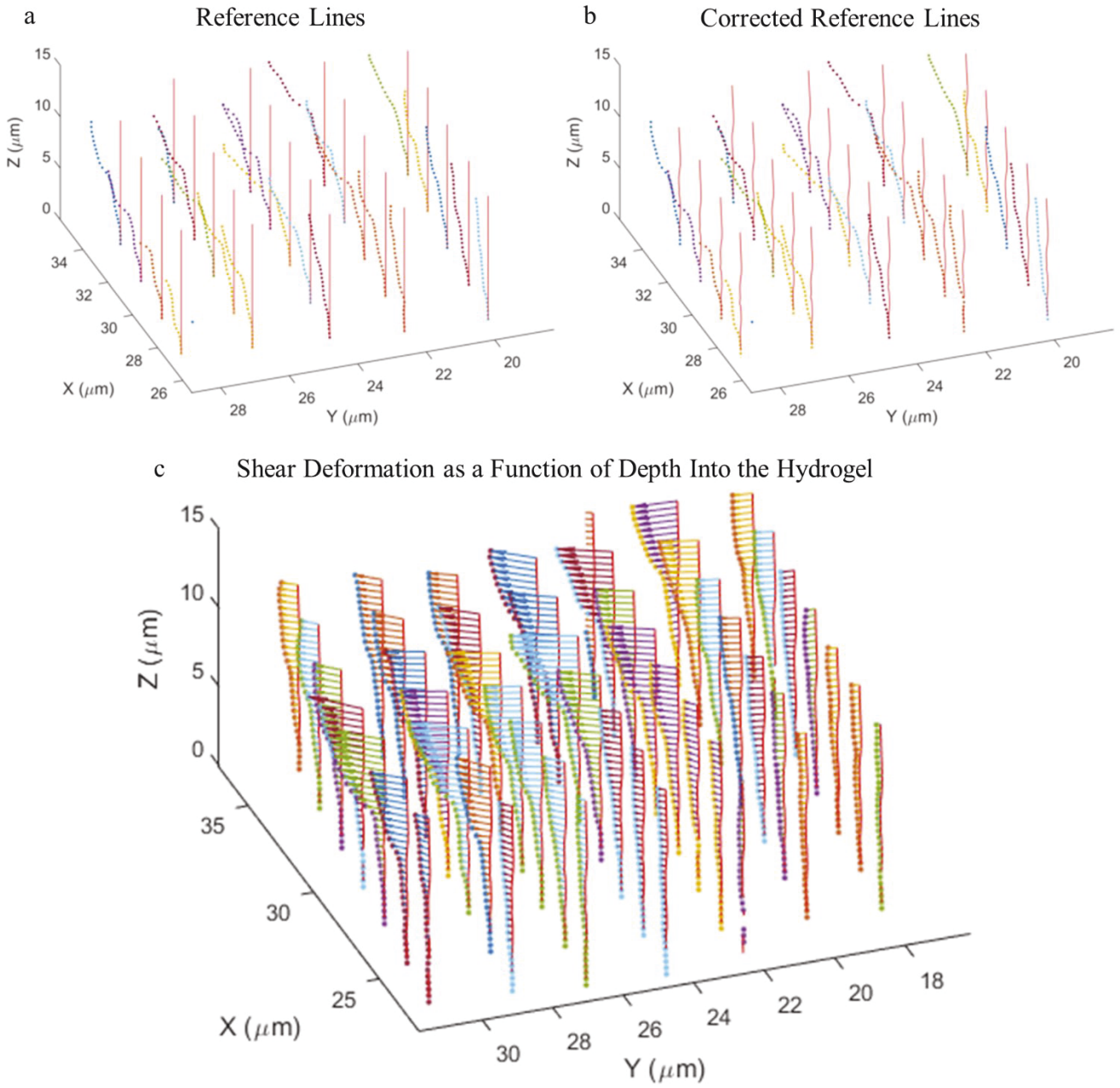

Figure S6. Determining the reference state and measuring shear deformation. (a) Initial XY reference coordinates are determined from the XY locations of the deepest markers in the array; furthest from the surface of the hydrogel. (b) The reference coordinates are corrected for tilt and others errors that occur in the patterning process, such as shifts in the X-direction in some rows. (c) Shear deformation within the hydrogel is measured as a function of depth from the hydrogel surface.

Object Detection for 3D Displacements: 3D subpixel localization of marker centroids within a Z-stack were detected using custom Matlab scripts (feature3dMB.m, llmx3dMB.m, fracshift3dMB.m, lrsqd3dMB.m; Yongxiang Gao and Maria Kilfoil 2005, based on IDL code by John C. Crocker and David G. Grier 1999.[5–7]), which are based on finding local maxima of intensity in the 3D image stack and include features such as a minimum separation distance between detections and a minimum intensity value to qualify as a detection. Subpixel localization is accomplished by approximating a center of mass (of inten sity) from an interpolated subarray centered around each detection with subarray dimensions related to the approximate expected radius of detections input by the user (**Figure S7**).

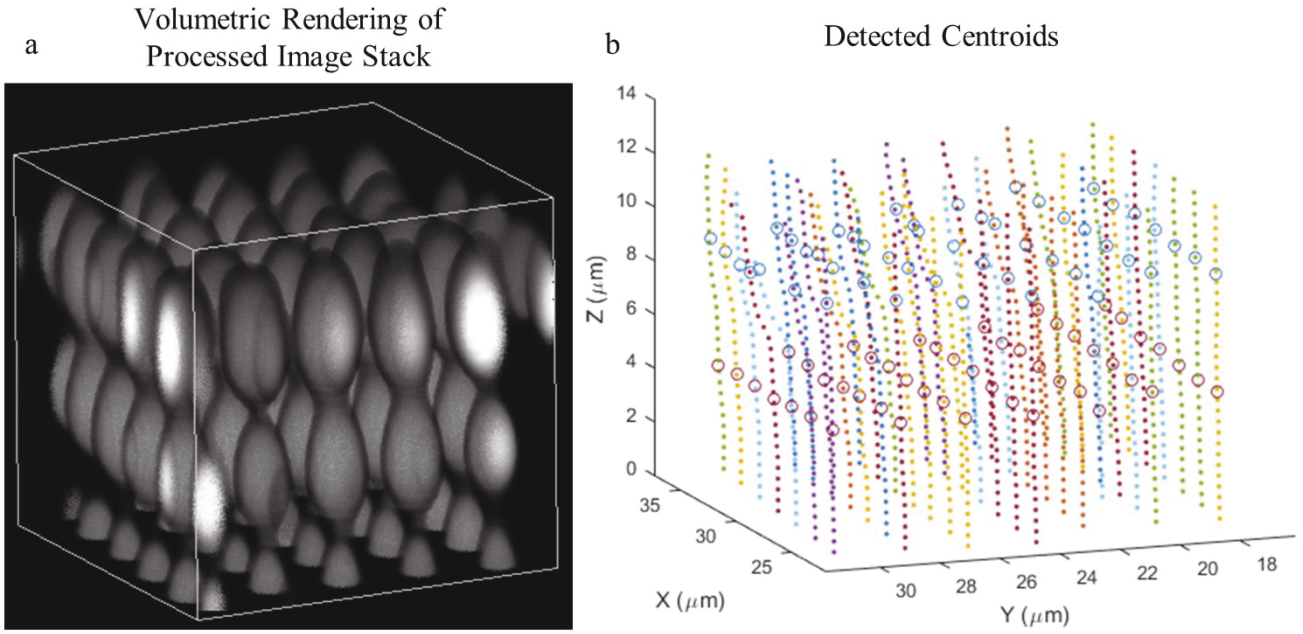

Figure S7. 3D centroid detection. (a) A volumetric rendering of a small volume of a processed image stack. (b) To obtain accurate 3D deformation measurements, the centroids of ellipsoids were detected. Ellipse centroids (circles) are plotted over previous shear detections (dots).

Object Linking through the X-Dimension (Rows): Limitations in the number of single pixel regions that could be loaded in the LSM software forced the feature arrays to be scribed line-by-line, with each line (100 features) being printed several times through the Z-direction before the stage shifted in the X-

direction to the next frame. Y-direction shifts occurred after all Z-planes in each frame through the X-direction at a given Y coordinate were scribed. As an overall result of this process, rows in the X-direction (printed all at once by the scanning galvometers) had better Z-positioning precision than rows in the Y-direction (printed one at a time with an automated stage shift between each). The array's X-dimension was determined algorithmically by identifying which array axis demonstrated a higher Z precision within non-deformed detections. Once determined, a characteristic row vector describing the slope of a non-deformed row was identified. Detections within a given plane were sequentially grouped into rows by starting with the coordinates of a seed detection, adding or subtracting a vector parallel to the row vector with length 2.12 μm, and creating a search window near the new location to find the closest candidate detection to be added to the same row; this process was repeated until no new detections were found for a given row, and then a new seed detection was chosen, and the process was repeated (**Figure S8a**).

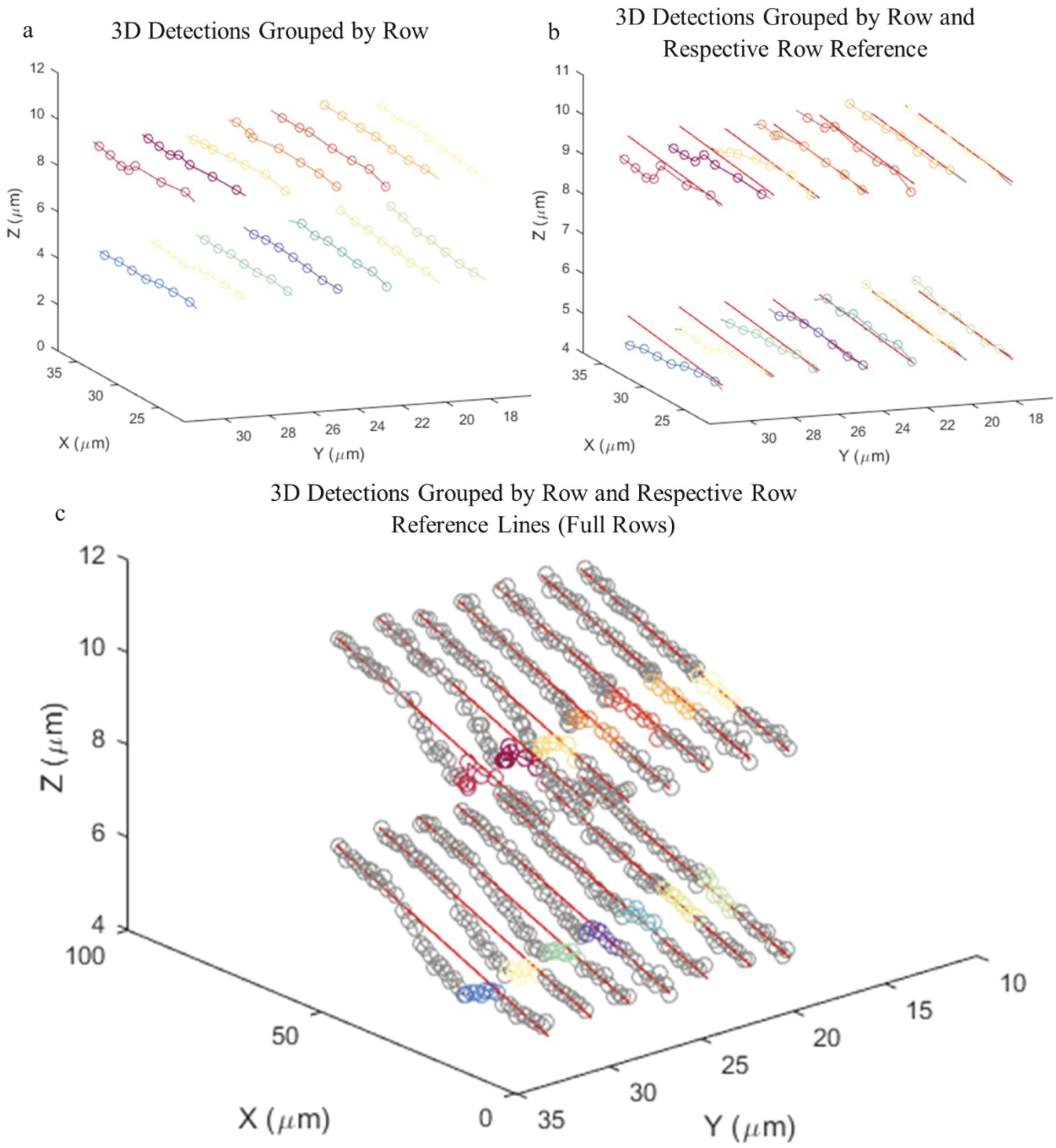

Figure S8. Grouping object detections by row. (a,b) Detections were grouped into rows in the X-direction to generate reference lines. (b) Detections and row traces are plotted in matching colors, and reference lines plotted in red. (c) The full rows, including non-deformed detections, help visualize the quality of row fits.

Approximating Z Reference Locations to Measure Displacement: Detections were grouped based on whether they were likely to be displaced. This distinction was made by digitally dilating a binary mask of a cell boundary by ~ 8μm (which was deemed a sufficient distance from a cell boundary to no longer register deformation), and designating all features occurring outside of the mask as unlikely to be displaced. Detections occurring within the XY coordinate space of the dilated cell boundary were identified and ignored during the linear fits used to determine reference coordinates.

X and Y reference coordinates for 3D detections were determined by identifying which column each detection belonged to and assigning the appropriate corrected XY reference coordinates. For approximating Z reference coordinates, two separate approaches were employed. *Method 1*. The default approach used non-deformed detections within a row to generate a best-fit line assumed to pass through all reference coordinates. From this line, Z reference coordinates were then approximated by finding the closest matching XY coordinates on the fit line to the XY reference coordinates and solving for the Z reference coordinate. This method worked well for rows where displaced features were flanked by non-displaced features in each region of interest, but did not work well in cases where there were too few non-displaced features. *Method 2*. To deal with exceptional cases of the second type, for each plane of detections, an average best-fit line was formulated based on the best-fit lines of rows meeting criteria for Method 1. The average best-fit line was then translated in 3D space to best fit non-displaced detections in rows which were not good candidates for fitting based on method 1, and had at least 1 non-displaced marker.

Once Z reference lines were determined, final 3D reference coordinates were approximated as the intersection between XY and Z reference lines (**Figure S9a**). Fiducial marker displacements were then

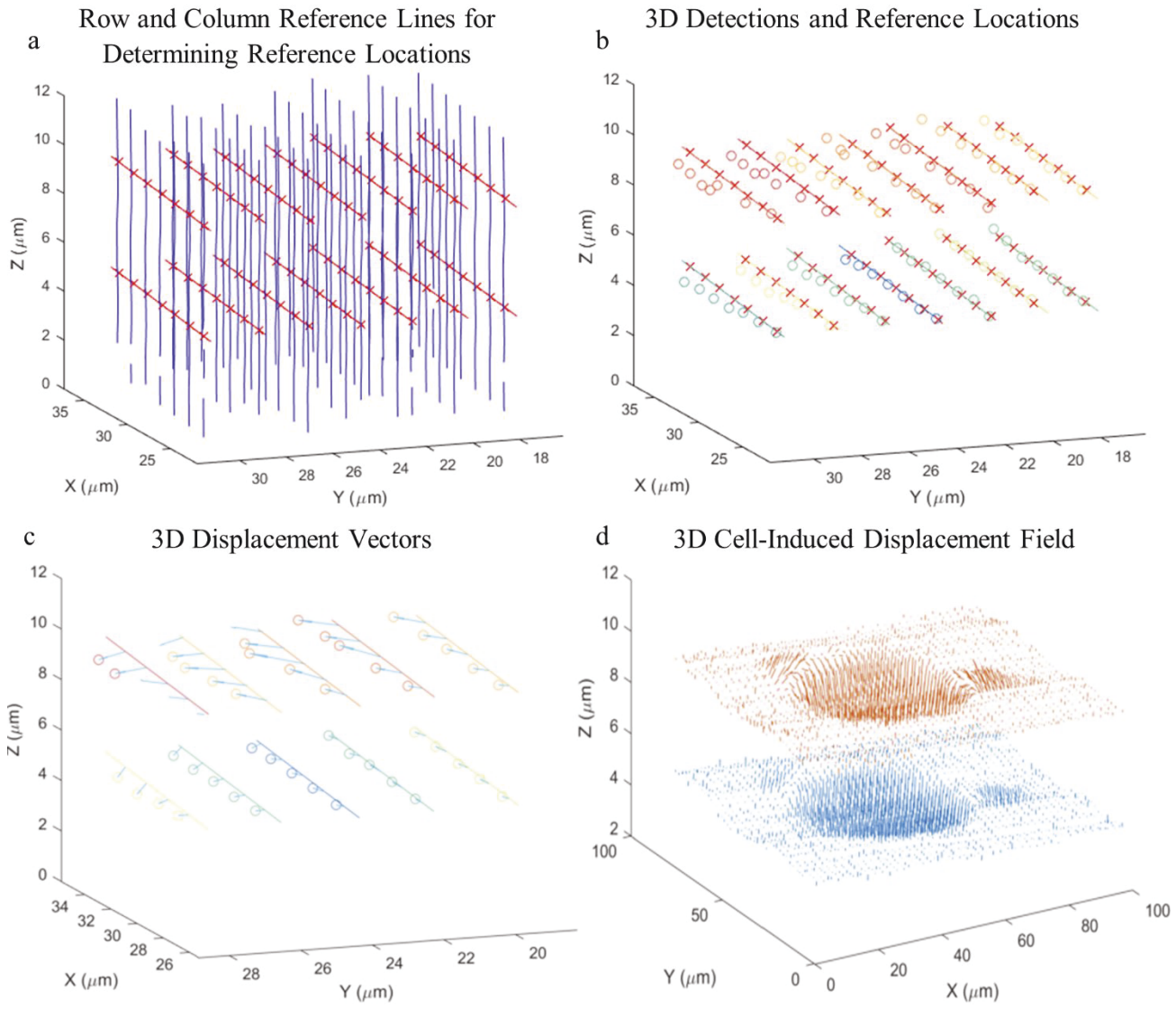

Figure S9. Measuring 3D displacement fields. (a) After grouping by row, 3D detections were also grouped by column based on previously determined reference locations. (b,c) The intersections of these reference lines were used to generate the 3D reference coordinates for each detection to measure 3D displacement. (d) An example displacement data set for a single cell is provided to visualize the overall 3D nature of collected deformation profiles.

calculated as the difference between these reference coordinates and fiducial marker centroids (Figure S9b-d).

Relating Shear and Normal Displacement Distributions

Line profiles of shear and normal displacements were created to visualize the spatial relationship between shear and normal components of tractions induced by HUVECs. The centroid of a binarized image of each cell's spread area was approximated based on a center of mass calculation. A line was traced from the centroid of the cell through the XY coordinates of the point of maximum shear displacement for each cell to create a displacement profile, averaged over a width of 3.25 μm in the XY plane about the trace. For each case, the shear displacement profile had an identifiable peak comprising tails proximal and distal to the cell periphery. To visualize many of these profiles simultaneously, the length of each trace was normalized such that the 20th and 80th percentile coordinates along the trace represented the locations where proximal and distal tails of the shear displacement peaks fell to 20% of the maximum, respectively (**Figure 5e**). Both shear and normal displacement profiles were normalized to the maximum shear displacement (**Figure 5f**). The mean profile for the entire dataset was generated to visualize overall trends in distribution. The mean location of the cells' edge within these profiles occurred near the center of the trace.

Interpolated Displacement Fields and Heat Maps

To visualize displacement fields measured within the hydrogels, the values of shear and normal displacement observed were interpolated using a bi-cubic interpolation scheme to generate displacement information at a pixel density equal to the resolution of the original images (6.153 pixel/μm). Interpolated data were used to determine the sum of shear or sum of normal deformations used in the analysis of shear and normal displacement relationships.

Statistical Information

All error bars and textual value ranges represent one standard deviation from the associated mean value. Linear regression models (**Figure 5**) were generated using the Matlab fitlm function, and the associated R^2, p-value, and sample size, n, are reported for each line. For some data, also reported are the x-coefficient representing the slope of the regression line.

References

(1) Cuchiara, M. L.; Horter, K. L.; Banda, O. a; West, J. L. Covalent Immobilization of Stem Cell Factor and Stromal Derived Factor 1α for in Vitro Culture of Hematopoietic Progenitor Cells. *Acta Biomater.* **2013**, *9* (12), 9258–9269. https://doi.org/10.1016/j.actbio.2013.08.012.

(2) Cruise, G. M.; Scharp, D. S.; Hubbell, J. a. Characterization of Permeability and Network Structure of Interfacially Photopolymerized Poly(Ethylene Glycol) Diacrylate Hydrogels. *Biomaterials* **1998**, *19* (14), 1287–1294.

(3) Majima, T.; Schnabel, W.; Weber, W. Phenyl-2,4,6-Trimethylbenzoylphosphinates as Water-Soluble Photoinitiators. Generation and Reactivity of O=P(C6H5)(O−) Radical Anions. *Die Makromol. Chemie* **1991**, *192* (10), 2307–2315. https://doi.org/10.1002/macp.1991.021921010.

(4) Banda, O. A. Slater Lab Git Hub Repository https://github.com/obanda310/Slater-Lab.

(5) Gao, Y.; Kilfoil, M. L. Accurate Detection and Complete Tracking of Large Populations of Features in Three Dimensions. *Opt. Express* **2009**, *17* (6), 4685. https://doi.org/10.1364/OE.17.004685.

(6) Crocker, J. C.; Grier, D. G. Methods of Digital Video Microscopy for Colloidal Studies. *J. Colloid Interface Sci.* **1996**, *179* (1), 298–310. https://doi.org/10.1006/jcis.1996.0217.

(7) http://people.umass.edu/kilfoil/downloads.html.